

Daytime and nighttime aerosol soluble iron formation in clean and slightly-polluted moisture air in a coastal city in eastern China

Wenshuai Li^{1,2}, Yuxuan Qi^{1,2}, Yingchen Liu^{1,2}, Guanru Wu^{1,2}, Yanjing Zhang^{1,2}, Jinhui Shi³, Wenjun Qu^{1,2}, Lifang Sheng^{1,2}, Wencai Wang^{1,2}, Daizhou Zhang⁴, Yang Zhou^{1,2}

¹Frontier Science Center for Deep Ocean Multispheres and Earth System (FDOMES) and Physical Oceanography Laboratory, Ocean University of China, Qingdao 266100, China.

²College of Oceanic and Atmospheric Sciences, Ocean University of China, Qingdao 266100, China.

³College of Environmental Science and Engineering, Ocean University of China, Qingdao 266100, China.

⁴Faculty of Environmental and Symbiotic Sciences, Prefectural University of Kumamoto, Kumamoto 862-8502, Japan.

Correspondence to: Daizhou Zhang (dz Zhang@pu-kumamoto.ac.jp) and Yang Zhou (yangzhou@ouc.edu.cn)

Abstract. Photocatalytic reactions during the daytime, alongside aqueous-phase reactions occurring during both daytime and nighttime, are identified as the two primary processes facilitating the conversion of aerosol iron (Fe) from the insoluble state to the soluble state within the atmospheric environment. This study investigated the levels of total Fe (Fe_T) and soluble Fe (Fe_S) in $PM_{2.5}$ samples collected during daytime and nighttime in Qingdao, a coastal city in eastern China, evaluating the distinctive roles of these two pathways in enhancing aerosol Fe solubility ($\%Fe_S$, defined as the ratio of Fe_S to Fe_T). Under clean and humid conditions, characterized by prevailing sea breezes and a relative humidity (RH) typically above 80%, an average daytime $\%Fe_S$ of 8.7% was observed, which systematically exceeded the nighttime $\%Fe_S$ (6.3%). Photochemical conversions involving oxalate contributed to the higher $\%Fe_S$ observed during daytime. Conversely, in scenarios where air masses originated from inland areas and exhibited slightly polluted, daytime $\%Fe_S$ (3.7%) was noted to be lower than the nighttime $\%Fe_S$ (5.8%). This discrepancy was attributable to the variations in RH, with nighttime RH averaging around 77%, conducive to the more efficient generation of acidic compounds, thereby accelerating Fe_S production compared to the daytime, when RH was only about 62%. Furthermore, the oxidation rates of sulfur (SOR) displayed a strong correlation with RH, particularly when RH fell below 75%. A 10% increase in RH corresponded to a 7.6% rise in SOR, which served as the primary driver of the higher aerosol acidity and $\%Fe_S$ at night. These findings highlight the RH-dependent activation of aqueous-phase reactions and the augmentation of daytime photocatalysis in the formation of Fe_S in the coastal moisture atmosphere.

30 **1 Introduction**

31 Iron (Fe) plays a pivotal role as a micronutrient in marine ecosystems, being a critical component of atmospheric
32 aerosol particles (Martin et al., 1994). Its deposition in high-nitrate, low-chlorophyll (HNLC) regions can trigger
33 phytoplankton bloom, thus enhancing atmospheric carbon absorption and fixation in seawater (Watson et al., 1994;
34 Watson and Lefèvre, 1999; Toner, 2023). Notably, only the soluble fraction of Fe (F_{es}) in aerosols, referred to as
35 bioavailable Fe, is accessible to phytoplankton (Zhuang et al., 1992; Sugie et al., 2013; Li et al., 2017). The
36 proportion of F_{es} to the total aerosol Fe (F_{T}), i.e., the aerosol Fe solubility ($\%F_{es}$), is influenced by the aerosols'
37 sources and the chemical conversion of Fe from insoluble forms to soluble forms in the atmosphere. $\%F_{es}$ in fresh
38 dust particles is typically below 1%, yet can exceed 10% in aerosols derived from combustion processes, such as
39 fly ash from coal and oil combustion (Oakes et al., 2012; Shi et al., 2012; Wang et al., 2015; Li et al., 2022).
40 The $\%F_{es}$ in primary particles can significantly increase due to atmospheric processes, primarily through aerosol
41 acidification via aqueous-phase reactions or photochemical conversions of precursors of acidic species (Solmon
42 et al., 2009; Shi et al., 2015; Li et al., 2017; Hettiarachchi et al., 2019), affecting the deposition flux of aerosol F_{es}
43 over the open ocean (Chen and Siefert, 2004; Shi et al., 2013; Yang et al., 2020).

44 Solar radiation and ambient humidity are two key meteorological factors that greatly influence the processes of
45 aerosol acidification. Solar irradiation induces photochemical reactions during daytime, leading to the formation
46 of free radicals and accelerating the production of acidic species within aerosols, thereby facilitating Fe dissolution
47 (Chen and Grassian, 2013; Liu et al., 2021b). Studies such as Fu et al. (2010) have demonstrated increased F_{es} in
48 dust samples exposed to light in the HCl solution. Furthermore, daytime photolysis of Fe-organic complexes is
49 another pathway for F_{es} formation, contributing to increased $\%F_{es}$ (Weller et al., 2014; Zhang et al., 2019; Zhou
50 et al., 2020). For example, Zhou et al. (2020) and Zhang et al. (2019) reported that photolysis of oxalate-Fe(III)
51 complex can result in the degradation of oxalate, enhancing Fe dissolution in aerosol particles during daytime.
52 These mechanisms have been supported by laboratory experiments and model simulations (Zhu et al., 1993; Chen
53 and Grassian, 2013; Sorooshian et al., 2013; Pang et al., 2019; Li et al., 2021). In contrast, high ambient relative
54 humidity (RH) can facilitate the heterogeneous/liquid phase formation of sulfate and nitrate during nighttime,
55 increasing aerosol acidity and promoting acids-associated Fe dissolution (Liu et al., 2020; Pye et al., 2020; Wong
56 et al., 2020). Studies like Zhang et al. (2022) observed enhanced $\%F_{es}$ ($>1\%$) at high RH levels ($>60\%$) in winter,
57 while Zhu et al. (2020) highlighted the greater impact of SO_4^{2-} and NO_3^- on $\%F_{es}$ at RH above 50%. Shi et al.

58 (2020) noted efficient Fe_s formation under foggy conditions, where SO_4^{2-} and NO_3^- concentrations were high due
59 to the absorption of precursor gases on wet particle surfaces, facilitating further water vapor absorption, and Fe_s
60 increase.

61 Aqueous-phase processes can occur during both daytime and nighttime, given adequate moisture. The formation
62 of Fe_s results from the interplay between photochemistry and aqueous chemistry during daytime, whereas it relies
63 solely on aqueous chemistry at night. The synergistic mechanisms and their individual contributions to Fe_s
64 formation remain partially understood.

65 To elucidate the roles of aqueous-phase and photochemical reactions on Fe_s formation, we collected $\text{PM}_{2.5}$ samples
66 during daytime and nighttime, separately, in a Chinese coastal city (Qingdao). Positioned under the westerlies of
67 the Northern Hemisphere, Qingdao acts as a primary conduit for East Asian terrestrial aerosols to the Northwestern
68 Pacific. Our research focuses on ascertaining the % Fe_s enhancement under clean and slightly-polluted air
69 conditions, reflecting typical coastal air quality. The primary goal is to delineate the contributions of aqueous-
70 phase reactions and photochemical processes to % Fe_s enhancement, thereby elucidating the dynamics of Fe
71 dissolution within the atmospheric chemistry of coastal areas.

72 **2 Methodology and materials**

73 **2.1 Sample collection and classification**

74 The observation was carried out on the following dates: April 24th to May 27th, 2017; March 28th to April 30th,
75 2018; and May 22nd to 28th, 2018. Two high-volume $\text{PM}_{2.5}$ samplers (TISCH, TE-6070BLX-2.5, USA) were
76 applied to collect $\text{PM}_{2.5}$ onto quartz microfiber filters (QM-A, PALL) and Whatman[®] 41 filters, respectively, on
77 the roof of Baguanshan Atmospheric Research Observatory (BARO, 36°03' N, 120°20' E, 76 m asl.). BARO is
78 located on the top of a small hill in the urban area of Qingdao, and around 0.7 km away from the coastline of the
79 Yellow Sea (Figure S1). $\text{PM}_{2.5}$ samples were collected separately during daytime and nighttime. Field blank
80 samples were also collected during the campaign by placing filters in the samplers with the samplers switched off.
81 After the sampling process, $\text{PM}_{2.5}$ samples were sealed and stored at -20°C before analysis.

82 For the measurement of water-soluble ions (WSIs) and carbonaceous matters, aerosol samples collected on QM-
83 A filters were utilized. The samples collected on Whatman[®] 41 filters were used for the detection of elements.
84 Firstly, samples were cut into pieces and immersed in Milli-Q pure water. Then, water-soluble matters were
85 extracted by ultrasonic vibration at approximately 0°C for 40 min. The water extracts were then filtered through

86 syringes with 0.45 μm strainer heads (PALL). The filtered extracts were analyzed for WSIs, including Na^+ , NH_4^+ ,
87 K^+ , Mg^{2+} , Ca^{2+} , F^- , Cl^- , SO_4^{2-} , NO_3^- , $\text{C}_2\text{O}_4^{2-}$, using ion chromatography (IC, Dionex ICS-3000, Dionex Corp.,
88 Sunnyvale, CA, USA). Similar sample pretreatment procedures were used to determine soluble elements. While,
89 10 ml of filtrate was taken and 0.187 ml HNO_3 (mass fraction: 69%) was added to water extracts before measuring
90 soluble elements, in case soluble Fe(II) was oxidized into an insoluble state. To determine total elements, sample
91 pieces were placed into inner-tanks and subjected to digestion with a mixture of HNO_3 + HF (at a volume ratio of
92 4:1) at 180°C for 48 h. The element concentrations were measured using inductively coupled plasma mass
93 spectrometry (ICP-MS, Model: iCAP Qc, Thermo Fisher Scientific Inc., Germany). Carbonaceous materials,
94 specifically organic carbon (OC) and elemental carbon (EC), were analyzed using a sunset OC/EC analyzer from
95 Sunset Laboratory Inc. The detection limits of the analysis instruments used can be found in Table S1. The organic
96 matter (OM) content was estimated with 1.6 times OC, as proposed by Turpin and Lim (2001). Further details
97 about sample collection, pretreatment procedures, and chemical species detection can be found in our previous
98 work (Li et al., 2023a; Li et al., 2023b).

99 Various weather conditions and air pollution characteristics were encountered during the observation period,
100 including clean, slightly-polluted (SP), heavily-polluted, foggy, and dusty conditions. Due to the large deviations
101 and uncertainties in the statistical results of dust-related samples, data from these samples were not considered.
102 Additionally, samples from heavily-polluted periods ($N = 6$, defined by $\text{PM}_{2.5} > 50 \mu\text{g m}^{-3}$ and $\text{PM}_{2.5}/\text{PM}_{10} > 0.4$)
103 and fog-influenced samples ($N = 12$) were also not included because of the limited sample number and the
104 significant difference in fog durations between samples. In this paper, we focus on the results of the clean period
105 samples ($N = 19$) and the SP period samples ($N = 32$). Clean periods samples were collected when $\text{PM}_{2.5} < 30 \mu\text{g}$
106 m^{-3} and $\text{PM}_{10} < 50 \mu\text{g m}^{-3}$. The SP periods samples were those collected when $30 \mu\text{g m}^{-3} < \text{PM}_{2.5} < 50 \mu\text{g m}^{-3}$ and
107 those collected when $\text{PM}_{2.5} < 30 \mu\text{g m}^{-3}$ while $\text{PM}_{10} > 50 \mu\text{g m}^{-3}$.

108 **2.2 Aerosol pH and liquid water content**

109 ISORROPIA (version II) thermodynamic equilibrium model was employed to estimate gas concentrations and
110 aerosol water pH (Song et al., 2018). The forward mode, which uses both gas and aerosol data as model input, was
111 utilized for pH calculations. This approach was preferred to the reverse mode because the later, using only aerosol
112 data, is very sensitive to the uncertainties of the measured WSIs concentrations (Hennigan et al., 2015; Song et al.,
113 2018). “Metastable-mode” was employed in ISORROPIA, assuming that solid precipitates did not form except for

114 CaSO₄. The concentrations of gaseous species (i.e., NH₃(g), HNO₃(g), HCl(g)) were not measured at the site. In
 115 alignment with the approach proposed by Sun et al. (2018), we devised a strategy to estimate the concentrations
 116 of these gaseous species. Initially, the input of aerosol data was assumed as the sum of aerosol and gas data
 117 (specifically for HNO₃, HCl and NH₃). This step provided us with the first set of gas and aerosol data outputs. For
 118 the second run, the gas data output derived from the initial run was added to the original aerosol data, and it was
 119 considered as the sum of gas data and aerosol data just like the first run to calculate HNO₃(g), HCl(g) and NH₃(g).
 120 The same method was employed for subsequent iterations until the variance in the NO₃⁻ output below the 1%
 121 threshold in mass. The calculation processes can be described by the following equations:

$$122 \quad \text{Input}[C_{\text{Aerosol}}+C_{\text{Gas}}]_{N+1}=C_{\text{Aerosol}}+[C_{\text{Gas}}]_N \quad (1)$$

$$123 \quad L = \left| \frac{[C_{\text{NO}_3^-}]_{N+1} - [C_{\text{NO}_3^-}]_N}{[C_{\text{NO}_3^-}]_N} \right| \times 100\% \quad (2)$$

124 where C_{Aerosol} is the observed concentration of NO₃⁻ (or NH₄⁺, Cl⁻), C_{Gas} is the concentration of gaseous species
 125 of HNO₃(g) (or NH₃(g), HCl(g)), and [C_{Gas}]_N is the concentration of gaseous species of HNO₃(g) (or NH₃(g),
 126 HCl(g)) output by ISORROPIA in the Nth run (N ≥ 1). The iteration was stopped until L < 1%.

127 Finally, three times of iterations (N_{max} = 3) were determined when L = 0.1%. The aerosol pH was calculated by
 128 using aqueous H⁺ concentration and aerosol liquid water content (ALWC) outputted by ISORROPIA, as described
 129 by equation (3).

$$130 \quad \text{pH} = -\log_{10} \frac{1000 \times \text{H}^+(\text{aq})}{\text{ALWC}} \quad (3)$$

131 Significant correlations between the results of the first run and the fourth run were observed for pH (r² = 0.95) and
 132 ALWC (r² = 0.99), indicating the stability and reliability in estimating the pH and ALWC by ISORROPIA II
 133 (Figure S2). Moreover, the correlations of NO₃⁻ (r² = 0.71), NH₄⁺ (r² = 0.98) and Cl⁻ (r² = 0.51) between the
 134 simulated results and measured concentrations are significant, demonstrating the robust confidence level of the
 135 simulated results (Figure S3).

136 In addition, the impact of organic matter (OM) on aerosol pH was determined to be minimal. This can be attributed
 137 to the limited sensitivity of the predicted pH to the water uptake by organic species (ALWC_{org}) when the OM
 138 fraction in PM_{2.5} is low (Guo et al., 2015; Liu et al., 2017). Following the methods of Guo et al. (2015), we
 139 estimated ALWC_{org} and its influence on aerosol pH. Our analysis determined the ALWC_{org} to range between 0.83

140 and $3.31 \mu\text{g m}^{-3}$, constituting merely 2.6–9.8% of the total ALWC. Aerosol pH was about 0.03–0.08 higher when
141 considering OM, affirming the negligible effect of OM on aerosol pH (see Text S1 in the supporting information
142 for more details).

143 **2.3 Weather conditions and air quality data**

144 The publicly released temperature, RH, surface pressure, wind speed, and wind direction recorded every 10
145 minutes were obtained from a meteorological observatory of the Qingdao Meteorological Bureau (Figure S1).
146 Hourly mass concentrations of $\text{PM}_{2.5}$, PM_{10} , SO_2 , NO_2 , O_3 and CO were obtained from an adjacent air quality
147 monitoring station in the Shinan District of Qingdao City (Figure S1), which is managed by Ministry of Ecology
148 and Environment of the People's Republic of China (<http://www.mee.gov.cn/>).

149 To examine the relative abundance of chemical species in aerosols, we reconstructed the mass concentrations of
150 $\text{PM}_{2.5}$ by equation (4) using the obtained concentrations of WSIs, OM, EC and elements.

$$151 \quad \text{PM}_{2.5\text{R}} = \text{WSIs} + \text{OM} + \text{EC} + \text{Elements} + \text{Si} + \text{Ca} \quad (4)$$

152 where $\text{PM}_{2.5\text{R}}$ is the reconstructed $\text{PM}_{2.5}$, and WSIs consists of Na^+ , NH_4^+ , K^+ , F^- , Cl^- , SO_4^{2-} , NO_3^- and $\text{C}_2\text{O}_4^{2-}$. As
153 for elements, Mg, Al, V, Cr, Mn, Fe, Ni, Co, Cu, Zn, Ga, As, Se, Rb, Sr, Cd, Ba, Tl and Pb were considered. Si
154 and Ca concentrations were estimated based on the mass ratio of Si/Al (3.43) following the methodology described
155 by Huang et al. (2010) and the mass ratio of Ca/Al (0.80) suggested by Arimoto et al. (2004) and Wang et al.
156 (2011). Because the nearby monitoring station is closer to the sea and less affected by human activities (yellow
157 dot in Figure S1), the level of $\text{PM}_{2.5\text{R}}$ is higher than the observations from the monitoring station. But the trends of
158 variations of these two datasets were consistent, indicating the high confidence of the $\text{PM}_{2.5\text{R}}$ dataset. In addition,
159 any mention of ionic ratios or normalized parameters in the results and discussions of this paper indicates the data
160 was divided by $\text{PM}_{2.5\text{R}}$.

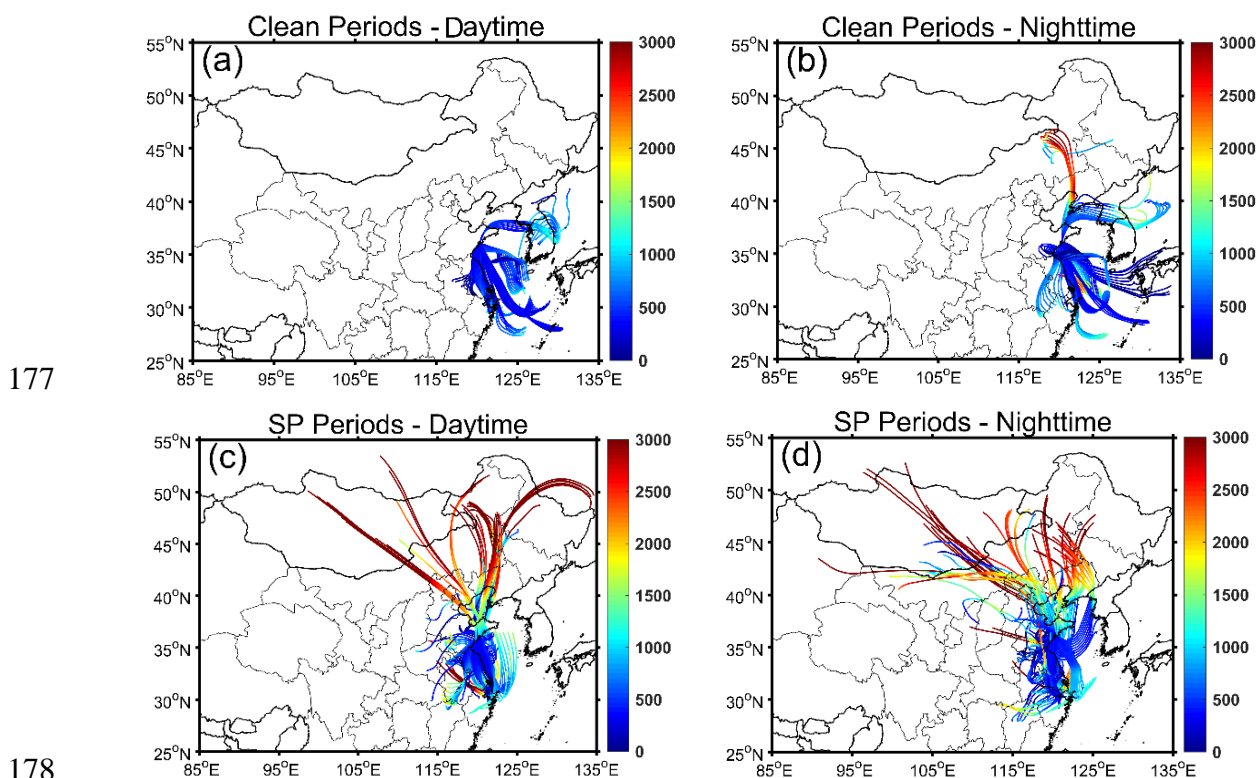
161 **2.4 Provenances of air masses**

162 The HYbrid Single-particle Lagrangian Integrated Trajectory (HYSPLIT) Model
163 (<https://www.ready.noaa.gov/HYSPLIT.php>), developed by NOAA, was applied to calculate the origins of air
164 masses from which $\text{PM}_{2.5}$ samples were collected. Gridded GDAS data with a horizontal resolution of $1.0^\circ \times 1.0^\circ$
165 were used as the input. Backward trajectories were computed for a period of 48 h, with starting points located at
166 300 m above ground level.

167 **3 Results**

168 **3.1 Meteorological features of clean and SP periods**

169 During clean periods, the backward trajectories reveal that the air masses mainly originated from sea areas (Figure
170 1). The prevailing sea breeze resulted in high RH levels of $81.5 \pm 4.9\%$ during daytime and $86.6 \pm 8.8\%$ during
171 nighttime (Table 1). The minimal temperature variance of less than 2°C between daytime and nighttime further
172 reflects the characteristics of marine atmosphere. In contrast, air masses during SP periods originated from various
173 directions, with a significant number traversing terrestrial regions prior to arriving at the collection site.
174 Temperature and RH exhibited noticeable diurnal variations. The daytime temperature was $17.2 \pm 3.0^\circ\text{C}$ and
175 decreased to $13.2 \pm 3.7^\circ\text{C}$ during nighttime. The RH levels were $62.1 \pm 9.4\%$ and $76.8 \pm 9.4\%$ during daytime and
176 nighttime, respectively.



179 **Figure 1: 48-h backward trajectories during daytime and nighttime during clean and slightly-polluted (SP) periods.**
180 **Trajectories are color-coded based on the altitude (unit: m) above the ground.**

181 **3.2 Concentrations of PM_{2.5} and Fe, and %Fes**

182 Table 1 presents the PM_{2.5} levels and aerosol Fe concentrations during both clean and SP periods. Under clean
183 conditions, PM_{2.5} concentrations were similar during daytime and nighttime, with average values of $16.9 \mu\text{g m}^{-3}$
184 and $16.4 \mu\text{g m}^{-3}$, respectively. Compared to the nighttime, Fe_T and Fe_S concentrations were higher during the

185 daytime, which were $289.2 \pm 223.4 \text{ ng m}^{-3}$ and $20.0 \pm 10.5 \text{ ng m}^{-3}$, respectively. Daytime levels of Fe_T and Fe_S
 186 were 1.5 times and 1.6 times as high as those observed at night, respectively. The increase in Fe_T and Fe_S during
 187 daytime may be linked to heightened human activities. Furthermore, the elevated Fe_S during daytime could be
 188 attributed to photochemical processes, which promoted the dissolution of aerosol Fe, a topic to be discussed further
 189 in Section 4.2. $\% \text{Fe}_S$ values ranged from 2.3% to 14.1% with an average of 8.7% during daytime, approximately
 190 1.4 times the nighttime average of 6.3% (after removing an extreme point of 37.2%).

191

192 **Table 1. Meteorological parameters, $\% \text{Fe}_S$, aerosol pH, the concentrations (average \pm standard deviation) of $\text{PM}_{2.5}$**
 193 **and chemical species during clean and slightly-polluted periods.**

	Clean Periods		Slightly-polluted Periods	
	Daytime	Nighttime	Daytime	Nighttime
$\text{PM}_{2.5}$ ($\mu\text{g m}^{-3}$)	16.9 ± 3.1	16.4 ± 5.6	30.3 ± 7.0	28.3 ± 7.7
Temperature ($^{\circ}\text{C}$)	16.6 ± 2.8	14.3 ± 2.3	17.2 ± 3.0	13.2 ± 3.7
RH (%)	81.5 ± 4.9	86.6 ± 8.8	62.1 ± 9.4	76.8 ± 9.4
ALWC ($\mu\text{g m}^{-3}$)	30.0 ± 13.5	55.0 ± 53.7	22.5 ± 13.2	44.1 ± 33.8
Fe_T (ng m^{-3})	289.2 ± 223.4	186.7 ± 122.2	938.3 ± 850.5	520.3 ± 496.1
Fe_S (ng m^{-3})	20.0 ± 10.5	12.5 ± 7.4	25.7 ± 10.5	21.6 ± 8.1
$\% \text{Fe}_S$ (%)	8.7 ± 3.8	6.3 ± 4.1	3.7 ± 2.0	5.8 ± 3.0
pH	0.46 ± 0.83	1.06 ± 0.96	1.16 ± 0.88	0.98 ± 0.75
SO_4^{2-} ($\mu\text{g m}^{-3}$)	13.97 ± 5.19	10.97 ± 8.06	14.94 ± 5.81	13.78 ± 5.43
$\text{F}(\text{SO}_4^{2-})^a$	$42.9\% \pm 14.0\%$	$36.8\% \pm 14.0\%$	$20.9\% \pm 3.6\%$	$23.0\% \pm 5.3\%$
NO_3^- ($\mu\text{g m}^{-3}$)	5.82 ± 3.49	5.63 ± 4.87	26.71 ± 13.15	22.80 ± 10.81
$\text{F}(\text{NO}_3^-)^b$	$15.7\% \pm 6.0\%$	$17.7\% \pm 11.3\%$	$35.4\% \pm 9.0\%$	$35.6\% \pm 9.0\%$
$(2[\text{SO}_4^{2-}] + [\text{NO}_3^-]) / \text{PM}_{2.5R}$ ($\mu\text{mol } \mu\text{g}^{-1}$)	0.0115 ± 0.0026	0.0105 ± 0.0023	0.0101 ± 0.0017	0.0106 ± 0.0016

194 ^a $\text{F}(\text{SO}_4^{2-})$ is the fraction of SO_4^{2-} in $\text{PM}_{2.5}$ mass, which was calculated by using SO_4^{2-} concentrations divided by $\text{PM}_{2.5R}$
 195 concentrations. ^b $\text{F}(\text{NO}_3^-)$ is the fraction of NO_3^- in $\text{PM}_{2.5}$ mass. The calculation method is the same as $\text{F}(\text{SO}_4^{2-})$.

196

197 Under SP conditions, $\text{PM}_{2.5}$ was at similar levels during daytime and nighttime with the average values of $30.3 \mu\text{g}$
 198 m^{-3} and $28.3 \mu\text{g m}^{-3}$, respectively. However, the daytime Fe_T ($938.3 \pm 850.5 \text{ ng m}^{-3}$) was much higher than the
 199 nighttime Fe_T ($520.3 \pm 496.1 \text{ ng m}^{-3}$), which was approximately threefold higher than during clean periods.
 200 Similarly, the daytime Fe_S concentration of $25.7 \pm 10.5 \text{ ng m}^{-3}$ was also slightly higher than the nighttime
 201 concentrations of $21.6 \pm 8.1 \text{ ng m}^{-3}$, which was 1–2 times higher than that during the clean period. Different from

202 the clean period, %Fes was markedly higher at night ($5.8\% \pm 3.0\%$) compared to the daytime %Fes ($3.7\% \pm 2.0\%$)
203 during the SP period, ranging from 1.0% to 12.3%.

204 3.3 Chemical characteristics of PM_{2.5}

205 Figure 2 illustrates the mass fractions of various chemical species present in the reconstructed PM_{2.5} (PM_{2.5R}).

206 During the clean period, WSIs were the dominant components, constituting about 75.0% and 74.1% of PM_{2.5} mass

207 during daytime and nighttime, respectively. SO₄²⁻, NO₃⁻, and NH₄⁺ were the main contributors to WSIs. During

208 daytime, SO₄²⁻ and NO₃⁻ were $13.97 \pm 5.19 \mu\text{g m}^{-3}$ and $5.82 \pm 3.49 \mu\text{g m}^{-3}$, respectively, serving as the major

209 acidic species and accounting for 42.9% and 15.7% of the PM_{2.5} mass (Table 1 and Figure 2). At night, SO₄²⁻ and

210 NO₃⁻ concentrations decreased slightly, which were $10.97 \pm 8.06 \mu\text{g m}^{-3}$ and $5.63 \pm 4.87 \mu\text{g m}^{-3}$, respectively,

211 representing 36.8% and 17.7% of the PM_{2.5} mass (Table 1 and Figure 2). In other words, the two main acid species,

212 SO₄²⁻ and NO₃⁻, occupied slightly larger fractions of the PM_{2.5} mass during the daytime (58.7%) compared to the

213 nighttime (54.6%), along with the lower ALWC, resulting in the lower aerosol pH of 0.46 ± 0.83 during daytime

214 (Table 1). At night, aerosol pH (1.06 ± 0.96) increased by a factor of 2.3 compared to daytime.

215 The aerosol pH calculated in this work was evidently lower than many other areas of China (Liu et al., 2017; Wang

216 et al., 2019; Xu et al., 2020). During the clean period, air masses mainly originated from the seas. Therefore, the

217 aerosol pH can be very acidic because of the lack of sources of alkaline substances over the ocean, such as NH₃,

218 Ca²⁺, et al. (Zhou et al., 2018). Compared to the inland areas, much lower aerosol pH in coastal areas is reasonable

219 (Wang et al., 2022). For instance, Zhou et al. (2018) reported that the pH of aerosols near the Bohai Sea can be as

220 low as around 1.0. Moreover, they also found that the daytime aerosol acidity was significantly stronger than that

221 during the nighttime in coastal areas. This observation aligns with the findings during clean periods in our study,

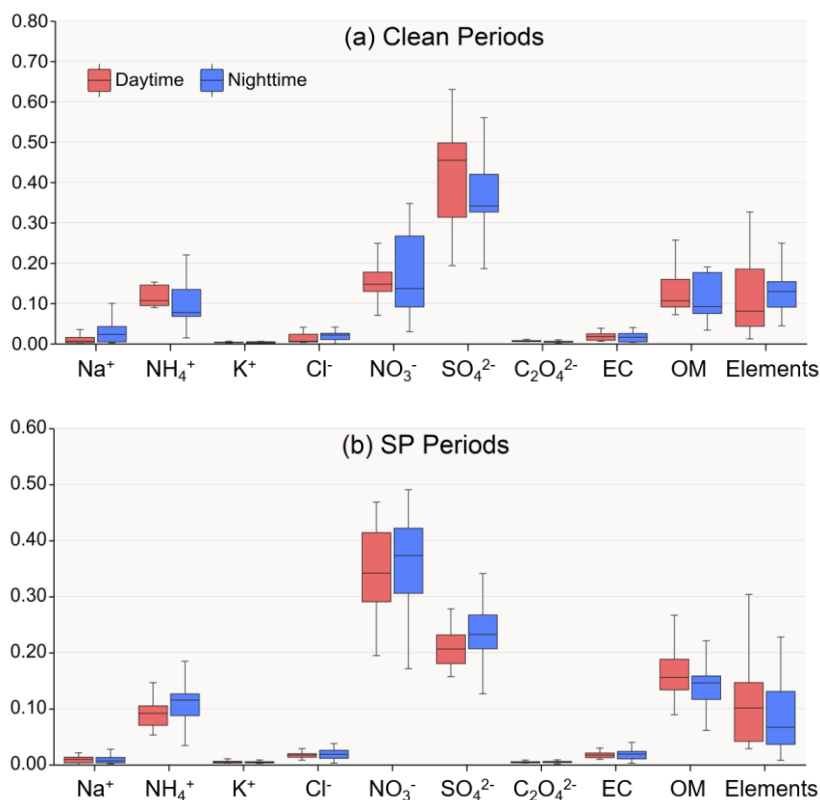
222 which were characterized by the predominance of sea breezes. In this study, we employed the ratio of acidic

223 substances to PM, namely, $(2[\text{SO}_4^{2-}] + [\text{NO}_3^-])/\text{PM}_{2.5R}$, to characterize the level of acidic substances in a unit of

224 PM_{2.5}, because SO₄²⁻ and NO₃⁻ were predominant acidic species within WSIs (>75% in mass). It was $0.0115 \pm$

225 $0.0026 \mu\text{mol } \mu\text{g}^{-1}$ and $0.0105 \pm 0.0023 \mu\text{mol } \mu\text{g}^{-1}$ in PM_{2.5} mass during daytime and nighttime, respectively (Table

226 1).



227

228

229 **Figure 2: Mass fractions of chemical species in reconstructed PM_{2.5} mass during daytime and nighttime in clean and SP**
 230 **conditions. Mg²⁺ and Ca²⁺ are not shown in the above pictures, because total Mg is included in elements data and total**
 231 **Ca is assessed by 0.8 times Al.**

232

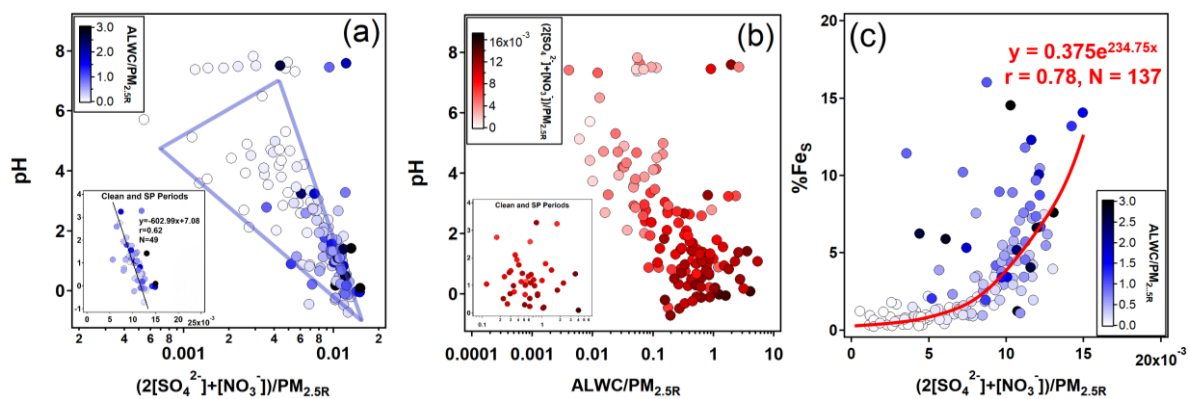
233 During the SP period, WSIs retained similar proportions in PM_{2.5} as during the clean period, accounting for 70.5%
 234 and 74.3% during daytime and nighttime, respectively. SO₄²⁻, NO₃⁻, and NH₄⁺ were also the main contributors to
 235 WSIs. In the daytime, the concentrations of SO₄²⁻ and NO₃⁻ were 14.94 ± 5.81 μg m⁻³ and 26.71 ± 13.15 μg m⁻³,
 236 respectively, showing a marginal elevation over nighttime levels (Table 1). However, SO₄²⁻ had evidently lower
 237 contributions to PM_{2.5} compared to the clean period, which were only 20.9% and 23.0% during daytime and
 238 nighttime, respectively (Table 1 and Figure 2). In contrast, NO₃⁻ had a noticeably higher contribution to PM_{2.5}
 239 compared to the clean period, exhibiting little diurnal variation, with percentages of 35.4% and 35.6% during
 240 daytime and nighttime, respectively (Table 1 and Figure 2). In total, the ratio of acids to PM (i.e.,
 241 (2[SO₄²⁻]+[NO₃⁻])/PM_{2.5R}) was 0.0101 ± 0.0017 μmol μg⁻¹ during daytime and 0.0106 ± 0.0016 μmol μg⁻¹ during
 242 nighttime (Table 1). Even though the ALWC (44.1 ± 33.8 μg m⁻³) was significantly more abundant at night
 243 compared to the daytime (22.5 ± 13.2 μg m⁻³), the aerosol pH was lower at night. Specifically, the nighttime
 244 aerosol pH was 0.98 ± 0.75, while the daytime aerosol pH was slightly higher at 1.16 ± 0.88, indicating weaker
 245 aerosol acidity during daytime with a 18.4% increase in pH compared to nighttime aerosols.

246 4 Discussion

247 We found that daytime %Fes was much higher than nighttime %Fes during the clean period, while the opposite
248 pattern emerged during the SP period. This section delves into the primary factors driving the distinct diurnal shifts
249 in aerosol %Fes during clean and SP periods, based on the aspects of aqueous-phase conversions and
250 photocatalysis reactions.

251 4.1 Aqueous-phase conversions promoted by acid processes

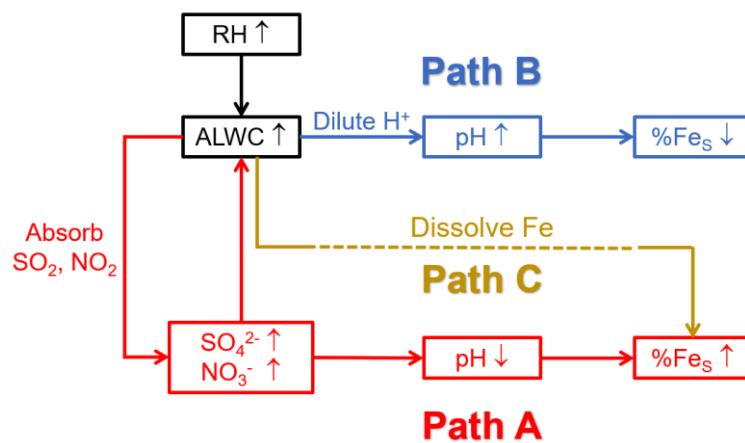
252 The %Fes was dependent on the acidification of the aerosol particles, and high %Fes was associated with low
253 aerosol pH (Table 1). The pH of aerosols is controlled by ALWC and H^+ contents. The predominant acidic species,
254 i.e., SO_4^{2-} and NO_3^- , play crucial roles in promoting the dissolution of insoluble Fe through proton-promoted
255 reactions. As shown in Figure 3a, there was a significant negative correlation between the aerosol pH and the
256 relative content of these two acidic species when the pH was below 4. Especially during clean and SP periods ($r =$
257 0.62, Figure 3a), the slope of the regression line was approximately -602.99 , indicating that a variation of 1.0 nmol
258 μg^{-1} of the acidic species content in $PM_{2.5}$ can lead to a noticeable fluctuation of aerosol pH (about 0.60). For
259 instance, the daytime aerosol pH was 0.60 lower than that of the nighttime during the clean period, even though
260 the difference of the two acidic species content was only about $1.0 \text{ nmol } \mu\text{g}^{-1}$.



261
262 **Figure 3: Relationships among pH, the normalized relative abundance of ALWC (unit: $\mu\text{g m}^{-3}$) and main acidic species**
263 **(= $2[SO_4^{2-}] + [NO_3^-]$, unit: $\mu\text{mol m}^{-3}$) with respect to the reconstructed $PM_{2.5}$ (i.e., $PM_{2.5R}$, unit: $\mu\text{g m}^{-3}$), and %Fes. The**
264 **subgraph at the bottom-left of figures (a) and (b) show scatter plots during clean and SP periods with the linear**
265 **regression line obtained by using the Igor Pro-based program developed by Wu and Yu (2018).**

266
267 There was no prominent correlation between pH and ALWC when the pH exceeded 6 (Figure 3b). When the pH
268 was smaller than 6, the increasing ALWC facilitated the heterogeneous reactions of SO_2 and NO_2 to generate more

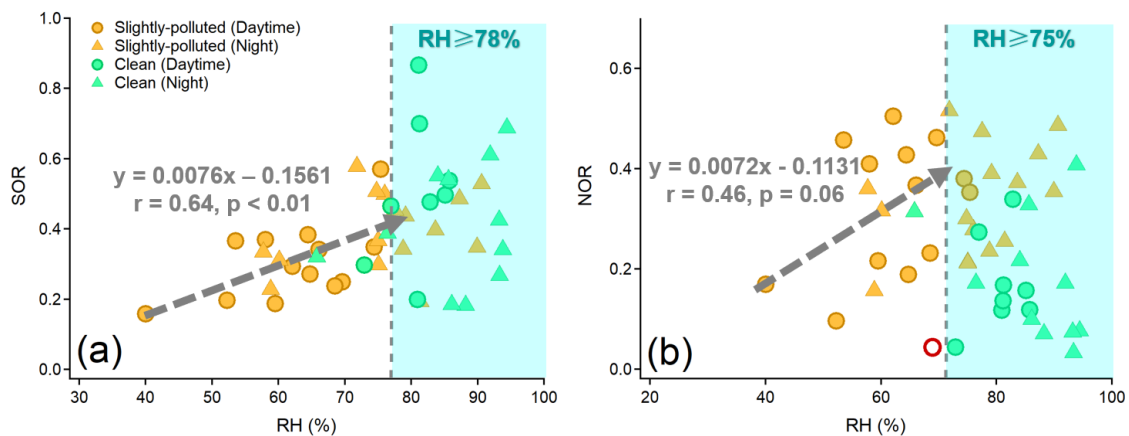
269 SO_4^{2-} and NO_3^- , lowering the aerosol pH and enhancing the %Fes. The formation of SO_4^{2-} and NO_3^- will further
 270 facilitate the growth of ALWC due to their remarkable hygroscopicity, establishing a positive feedback (Path A in
 271 Figure 4), referred to as the “ALWC-acid” feedback (Wang et al., 2016; Wu et al., 2018b). On the other hand,
 272 ALWC dilutes H^+ in aerosol water. This process weakens the aerosol acidity and inhibits the particles from %Fes
 273 elevation (Path B in Figure 4). In addition, the increasing ALWC served as a medium for loading water-soluble
 274 components may promote the formation of Fes (Path C in Figure 4). The profound influence of acidic species on
 275 the aerosol pH indicates the predominance of the “ALWC-acid” feedback in modulating the aerosol pH and
 276 augmenting %Fes (Figures 3a, 3c and S4). The high %Fes we observed during daytime and nighttime can be
 277 attributed to the relatively higher content of acidic species in $\text{PM}_{2.5}$.



278
 279 **Figure 4: Schematic diagram of ALWC affecting pH and %Fes. Path C is challenging to observe and quantify because**
 280 **of the Fes extraction using MilliQ water in the sample pretreatment.**

281
 282 RH is a key factor in the formation of SO_4^{2-} and NO_3^- through heterogeneous/aqueous-phase reactions within
 283 aerosols (Wang et al., 2016; Liu et al., 2020; Hou et al., 2022). As demonstrated in Figure 5, the strong dependency
 284 of the oxidation rate of sulfur (SOR, defined as $[\text{SO}_4^{2-}]/([\text{SO}_4^{2-}] + [\text{SO}_2])$) on RH was observed under moderate
 285 humid conditions ($r = 0.64$, $p < 0.01$). But the nitrogen (NOR, defined as $[\text{NO}_3^-]/([\text{NO}_3^-] + [\text{NO}_2])$) had a poor
 286 dependence on RH ($r = 0.46$, $p > 0.05$). A decrease of 10% in RH resulted in a notable reduction of 7.6% in SOR
 287 (Figure 5). Such a striking RH dependence was observed mainly during the SP period, indicating the significant
 288 role of heterogeneous reactions in controlling the formation of SO_4^{2-} . Therefore, the facilitation of aqueous-phase
 289 conversions leading to the formation of SO_4^{2-} was more pronounced at night during the SP period, attributed to
 290 the high RH. This, in turn, resulted in a high proportion of SO_4^{2-} and acidic species, as well as the elevated SOR

291 (Table 1, Figures 2b and S5). The nighttime aerosol pH was approximately 0.18 units lower than that during
 292 daytime, but this slight variation did not hinder the efficient formation of Fes during nighttime in SP periods.
 293 In contrast, RH was generally above 80% during daytime and nighttime in clean periods. The SOR was 0.49 on
 294 average and did not exhibit a clear correlation with RH beyond 78% (Figure 5a). Similar phenomena have been
 295 observed in previous studies, suggesting the existence of a saturation point in the promotion of RH on the aqueous-
 296 phase formation of SO_4^{2-} (Wang et al., 2019; Wang et al., 2021). High RH (> 70%) can cause water-soluble species
 297 to deliquesce and form an aqueous layer on the particle surface. Once the aqueous layer forms, the influence of
 298 RH variations becomes minimal (Shi et al., 2022). Hence, the degree of aqueous-phase processes promoting SO_4^{2-}
 299 formation during clean periods was similar across both daytime and nighttime.



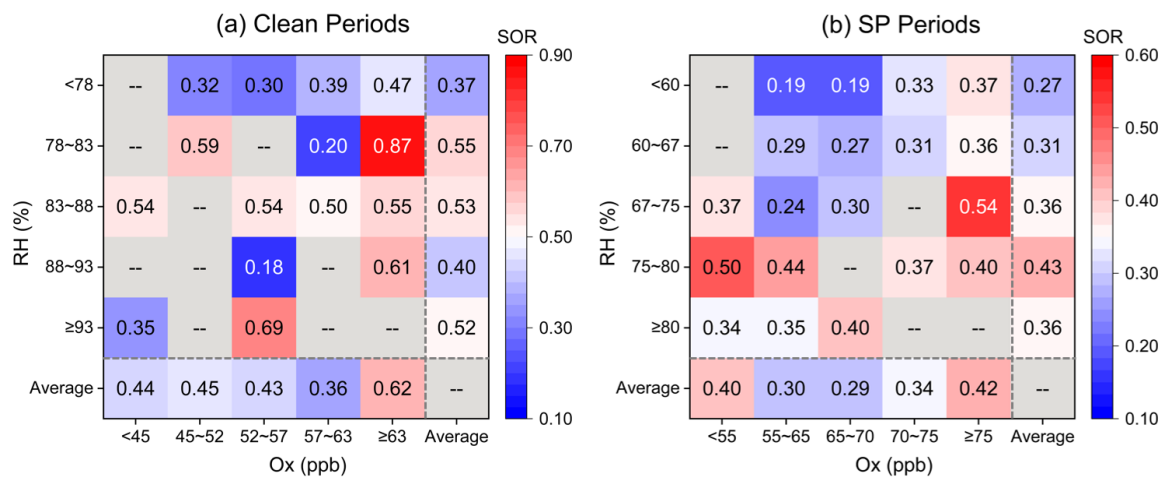
300
 301 **Figure 5: The dependence of SOR (a) and NOR (b) on RH during clean and slightly-polluted periods. The fitting of the**
 302 **regression line between SOR and RH was fitted when $\text{RH} < 78\%$. The fitting of the regression line between NOR and RH**
 303 **was fitted when $\text{RH} < 75\%$ and one deviation point (the red circle in (b)) was removed.**

304
 305 **4.2 Daytime enhancement by photocatalysis reactions**

306 **4.2.1 The influence of photochemical processes on sulfate formation**

307 Photochemical reactions can enhance the formation of acidic species and increase the aerosol %Fes through aerosol
 308 acidification (Tao et al., 2020; Liu et al., 2021a). The large proportion of acidic species during the daytime of the
 309 clean period was attributable to SO_4^{2-} , which was 6.1% higher than the nighttime SO_4^{2-} (Table 1 and Figure 2a).
 310 Despite similar levels of SO_2 observed during daytime and nighttime, the daytime SOR reached as high as $0.50 \pm$
 311 0.20 (Figure S5). The conversion rates in the aqueous phase were similar during daytime and nighttime in clean
 312 periods. Therefore, the substantial fraction of SO_4^{2-} was most likely caused by photochemical reactions.

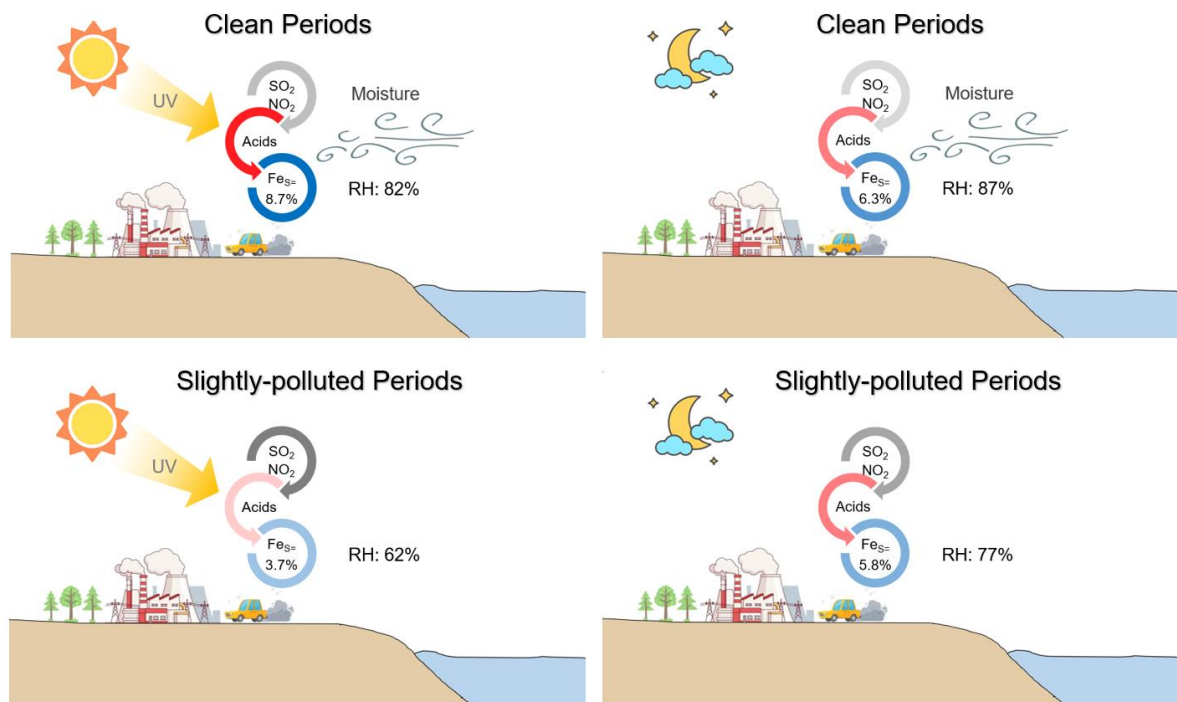
313 O_x (described by the sum of O_3 and NO_2) was investigated to quantify the potential of photochemical reactions,
 314 following the method of Wu et al. (2018a). The daytime O_x concentration (56.1 ± 6.4 ppb) was about 5.1% higher
 315 than that of nighttime O_x (53.4 ± 9.3 ppb) during the clean period. The substantial SOR occurred under the extreme
 316 O_x conditions (Figure 6a), suggesting a significant contribution of the photochemical reactions during the clean
 317 period. The enhancement of daytime photochemistry and aqueous chemistry on aerosol %Fes was more
 318 pronounced than that of the nighttime aqueous reactions solely during the clean period (Figure 7a and 7b).



319
 320 **Figure 6: RH- O_x image plots colored by SOR during clean and SP periods. The last row and last column of the matrices**
 321 **represent the average value of SOR in the corresponding ranges of RH and O_x .**

322
 323 During the SP period, the extent of SOR was more influenced by RH than by O_x , especially when RH was below
 324 80% (Figure 6b). Nighttime SOR (0.37 ± 0.12) was approximately 1.2 times higher than the daytime SOR ($0.31 \pm$
 325 0.11) even though the daytime O_x was higher than that during nighttime (Figure S5), indicating a greater
 326 contribution of liquid/heterogeneous reactions to the SO_4^{2-} formation than photocatalytic reactions. Similar
 327 findings were reported by Hou et al. (2022), who highlighted the dominant role of humidity rather than O_x in SO_4^{2-}
 328 formation in haze intensification. The nighttime exhibited a more significant "ALWC-acid" feedback compared to
 329 the daytime during the SP period. The influence of daytime photochemistry combined with aqueous-phase
 330 reactions was comparatively weaker than nighttime aqueous chemistry, leading to the higher %Fes at night (Figure
 331 7c and 7d). Notably, O_x concentrations were significantly higher during the SP period in comparison to the clean
 332 period (Figure S5), indicating more active daytime photocatalytic reactions. However, the impact of aqueous-
 333 phase conversions during the SP nighttime period was relatively weak compared to the nighttime of the clean

334 period. These results suggest that the role of photocatalytic reactions in SO_4^{2-} formation, and subsequently in the
335 elevation of aerosol % Fe_s , was feeble compared to aqueous-phase conversions.



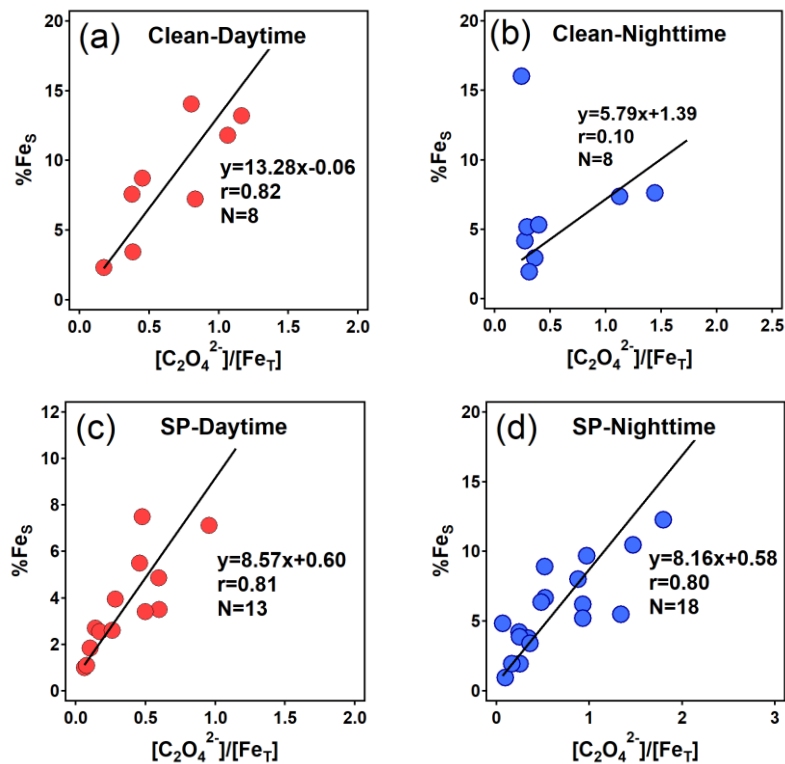
336
337 **Figure 7: Conceptual diagram showing the Fe dissolution influenced by acid processes at the coastal city during daytime**
338 **and nighttime in clean and SP periods.**

339
340 Enhancing aerosol % Fe_s through direct photocatalysis pathways is indeed possible. Iron oxides in minerals can
341 generate conduction band electrons upon irradiation, causing the reductive dissolution of Fe(III)-containing solid
342 phases to Fe(II) species (Zhang et al., 1993; Fu et al., 2010). However, structural Fe(III), which is the major iron-
343 related mineral in dust and coal fly ash, does not readily undergo direct reduction upon UV irradiation (Fu et al.,
344 2012; Fu et al., 2010; Xie et al., 2020). Another pathway for photolysis-conducted iron dissolution involves the
345 reduction by reactive oxygen species (ROS, e.g., O_2^- , HO_2^* , and H_2O_2). These ROS can be generated from
346 dissolved oxygen accompanied by conduction band electrons, enhancing the Fe dissolution by reducing the solid-
347 phase Fe(III) into the more soluble Fe(II) form (Zhu et al., 1997; Hettiarachchi and Rubasinghege, 2020). Aerosol
348 water is necessary for the above reactions, and the proton-promoted dissolution by acid species is indispensable to
349 dissolve the solid-phase Fe(II) into aerosol solutions. We suppose that the observed weak influence of
350 photocatalysis on % Fe_s was because of the extreme aerosol acidity. The acidity of aerosols, such as a pH as low
351 as 2.0 during daytime of the present study, can suppress the contribution of photochemical catalysis in the

352 formation of Fe_s (Zhu et al., 1993; Fu et al., 2010; Fu et al., 2012). In addition, studies have suggested that Fe
 353 dissolution can be inhibited in H_2SO_4 systems under irradiation compared to dark conditions, which could be
 354 another reason for the low $\% \text{Fe}_s$ during daytime although the exact mechanism remains unclear (Fu et al., 2010;
 355 Hettiarachchi et al., 2018).

356 4.2.2 The enhancement of $\% \text{Fe}_s$ promoted by oxalate-related conversions

357 Oxalate can form complexes with Fe(III) and participate in photochemical reactions through photoinduced charge
 358 transfer. Oxalate transfers its charge to the Fe(III) surface via photolytic reactions during daytime, resulting in the
 359 reduction of Fe(III) to Fe(II) , followed by the dissociation of the formed Fe(II) from the surface and hence the
 360 dissolution of aerosol Fe (Zuo and Hoigne, 1992; Zhang et al., 2019; Lueder et al., 2020). Shi et al. (2022)
 361 identified the oxalate/ Fe_T ratio as an excellent predictor for aerosol $\% \text{Fe}_s$ through machine learning, underscoring
 362 its remarkable effectiveness. However, field observations rarely confirm its influence on Fe_s from the perspective
 363 of oxalate- Fe photochemistry.



364

365

366 **Figure 8: Relationships between $\% \text{Fe}_s$ and the molar ratio (unit: $\mu\text{mol } \mu\text{mol}^{-1}$) of oxalate to Fe_T during daytime and**
 367 **nighttime in clean and SP periods. An extreme point (marked by a pink triangle, $\% \text{Fe}_s = 37.2\%$) in (b) was removed.**

368

369 In this study, significant correlations were observed between %Fes and the molar ratio of [oxalate]/[Fe_T] during
370 daytime in both clean periods ($r = 0.82$) and SP periods ($r = 0.81$) (Figure 8a and 8c). Similarly, a striking
371 correlation was also found in nighttime during the SP period ($r = 0.80$), although with a lower slope of 8.16 in the
372 regression line (Figure 8d). Noteworthy is the strong dependence of %Fes (or Fes) on oxalate concentration at
373 night (Figures 8d, S6b and S6d). Field observations highlight the pivotal role of organic compound complexation
374 in stabilizing Fe (Sakata et al., 2022). Additionally, as illustrated by Figure 8a and 8c, the variation in %Fes induced
375 by each unit variation in daytime [oxalate]/[Fe_T] was greater than its nighttime equivalent. The most notable
376 increase was observed during the clean period, with a daytime slope of 13.28, marking a 1.6-fold increase over the
377 SP period (daytime slope = 8.57). Similarly, the concentration of Fes per unit of oxalate showed a parallel trend,
378 marking the highest daytime slope of the clean period during the campaign (Figure S6). Such patterns imply that
379 enhanced sunlight in clean days may have catalyzed photochemical processes involving daytime oxalate-Fe,
380 leading to elevated concentrations of both Fes and %Fes. While these outcomes have only been discussed through
381 laboratory simulations (Chen and Grassian, 2013), or indirectly by examining oxalate degradation or sulfate
382 formation (Zhou et al. 2020), and they have been empirically discovered through field observations now in this
383 study.

384 Simultaneously, Fes species redox reactions can facilitate the formation of oxalate in return if the precursors are
385 abundant, particularly with aqueous-phase reactions playing a pivotal role when RH exceeds 60% (Zhang et al.,
386 2019). This may elucidate one of the main reasons behind the significant correlations observed between Fes and
387 oxalate. Notably, oxalate concentration was higher during the daytime compared to the nighttime in this study
388 (Figure S5), concomitant with elevated Fes concentrations. The photocatalytic degradation of oxalate-Fe,
389 promoting Fe dissolution during daytime, was unlikely to be the predominant pathway influencing the oxalate
390 concentration, otherwise a decrease in oxalate concentration would occur (Dou et al., 2021). Therefore, the oxalate
391 formation process catalyzed by Fes could yield a higher production rate of oxalate during the daytime than at night.
392 Figure S7 portrays the conceptual diagram of these conversion processes. Similar scenarios might unfold for SO₄²⁻
393 formation due to the heightened Fe redox reactions during daytime (Zhou et al., 2020). Owing to the extremely
394 low aerosol pH (< 2), transition-metal ions (TMIs, e.g., Fes)-catalyzed pathway could primarily influence the
395 secondary formation of SO₄²⁻, leading to potent aerosol acidity (Liu et al., 2021b). The elevated aerosol acidity, in
396 turn, fostered the formation of Fes, thus furthering the generation of SO₄²⁻ and oxalate under high RH conditions.
397 The resulting oxalate could then be complexed with Fes, sustaining %Fes at a high level at night.

398 To summarise, the findings of this study suggest that daytime photochemical processes indeed facilitated the
399 dissolution of aerosol Fe, consequently elevating %Fes during the clean period. This mechanism, in turn, may
400 foster the secondary formation of oxalate and SO_4^{2-} . The complexation of organic compounds significantly
401 contributed to maintaining the high %Fes at night. While during SP periods, the diurnal variation in aerosol %Fes
402 mainly resulted from the differing levels of aerosol acidity between daytime and nighttime, a conclusion strongly
403 supported by the higher %Fes observed at night compared to daytime.

404 **4.3 Environmental implications**

405 Limited research has explored the diurnal variation of aerosol %Fes. Only an early case investigated the diel
406 variability of Fe species at an island located in the Caribbean Sea and highlighted the photochemical processing
407 of Fe (Zhu et al., 1997). This study found a pronounced correlation between Fes and acid species within an aerosol
408 pH range of 0 to 1, emphasizing the considerable influence of aerosol acidification on Fe dissolution. These
409 findings align with the results of our study. Our results suggest that acid-driven aqueous-phase transformations
410 could have a more crucial role in altering aerosol %Fes than photochemical reactions under certain conditions in
411 coastal urban areas.

412 Previous studies pinpointed robust %Fes of anthropogenic aerosols, especially for combustion-related fly ash
413 (Oakes et al., 2012; Wang et al., 2015; Baldo et al., 2022; Li et al., 2022). Unlike urban air, RH tends to be
414 considerably higher over open oceans, fostering an environment where heterogeneous reactions and the secondary
415 formation of SO_4^{2-} and NO_3^- are prevalent. In such cases, photochemical reactions and precursors' concentrations
416 will determine the formation of salts. Given that the air mass of the clean period comprised a mix of marine and
417 local urban air, it is expected that the Fe dissolution in aerosol particles is an effective way to produce Fes during
418 daylight hours. Air masses moving from densely populated land areas carry substantial amounts of SO_2 , NO_2 and
419 NH_3 to offshore areas, aiding in the formation of SO_4^{2-} and NO_3^- and conducting to the acidic dissolution of Fe in
420 aerosol particles. Subsequently, the solubilized Fe, through proton-promoted dissolution, can be further stabilized
421 by the organic complexation of Fe in the marine atmosphere, as indicated by Sakata et al. (2022).

422 Additionally, the dearth of ammonia sources in the marine atmosphere may hinder the formation of SO_4^{2-} and
423 NO_3^- to some extent on the one hand (Wang et al., 2017; Guo et al., 2018). The limited availability of ammonia
424 may be also conducive to enhancing the aerosol acidity and elevating aerosol %Fes on the other hand. Considering
425 that concentrations of HCl in remote marine atmospheric boundary layer are typically higher than in the continent

426 of East Asia, the influence of chloride on aerosol pH may therefore play a conspicuous role in regulating %Fes
427 (Tobo et al., 2010), on which knowledge is very limited.

428 **5 Summary**

429 This study investigated the daytime and nighttime %Fes in PM_{2.5} in a coastal city of China under clean and SP
430 conditions. Under clean conditions, %Fes was higher during daytime (8.7%) compared to the nighttime (6.3%,
431 after removing an extreme point of 37.2%). On the contrary, under SP conditions, %Fes was higher at night (5.8%)
432 than during daytime (3.7%). Significant correlations were observed between the main acidic components (SO₄²⁻
433 and NO₃⁻), aerosol pH, and %Fes, indicating that the acid process played a dominant role in influencing
434 aerosol %Fes.

435 The RH consistently exceeded 80% during both daytime and nighttime in clean periods. Aqueous-phase reactions
436 were found to be most effective in promoting the secondary formation of acid species, with photochemical
437 processes further enhancing SO₄²⁻ formation during daytime. Together with the lower ALWC, the aerosol pH was
438 much lower during daytime (0.46 ± 0.83) compared to nighttime (1.06 ± 0.96) during the clean period, which
439 exerted a more significant influence on aerosol Fe dissolution. In contrast, RH was much higher at night (76.8%)
440 than that during daytime (62.1%) in the SP period. The dry conditions during daytime notably restricted the
441 secondary formation of SO₄²⁻ and NO₃⁻. The acid content in PM_{2.5} was much higher at night under the promotion
442 of heterogeneous processes, resulting in stronger aerosol acidity and higher aerosol %Fes. Furthermore,
443 photochemical reactions associated with oxalate likely played a considerable role in enhancing %Fes during
444 daylight hours, a trend more noticeable during the clean period. Oxalate might also be crucial in sustaining
445 elevated %Fes at night during the SP period.

446 This study provides insights into the mechanisms of aerosol %Fes modulation in the coastal city. The robust
447 promotion of aqueous-phase processes and the comparatively weaker influence of photochemistry on enhancing
448 aerosol %Fes were observed. In urban air, RH was a crucial factor in controlling %Fes through modulating the
449 heterogeneous reactions of SO₄²⁻ and NO₃⁻. In contrast, in the oceanic atmospheric boundary layer, precursors'
450 levels and photochemical processes may be the decisive manipulators on aerosol %Fes. Therefore, the content of
451 bioavailable Fe in urban-related aerosols may be greatly elevated after intrusion into the marine atmosphere, which
452 holds significant importance for future research.

453 **Author contributions.** WL: investigation, formal analysis, writing – original draft, writing – review and editing;
454 YQ: methodology; YL: methodology; GW: visualization; YZ: methodology; JS: methodology; WQ: methodology;
455 LS: supervision, funding acquisition; WW: methodology; DZ: funding acquisition, methodology, writing – review
456 and editing; YZ: conceptualization, funding acquisition, methodology, supervision, writing – review and editing.

457 **Acknowledgements.** We gratefully acknowledge the National Oceanic and Atmospheric Administration (NOAA)
458 Air Resources Laboratory (ARL) for the provision of the HYSPLIT transport and dispersion model, available at
459 (<https://www.ready.noaa.gov/HYSPLIT.php>), and the Global Data Assimilation System (GDAS). Additionally, we
460 acknowledge the use of ISORROPIA II, accessible at ([https://www.epfl.ch/labs/lapi/models-and-](https://www.epfl.ch/labs/lapi/models-and-software/isorrophia/)
461 [software/isorrophia/](https://www.epfl.ch/labs/lapi/models-and-software/isorrophia/)), developed by the Schools of Earth & Atmospheric Sciences and Chemical & Biomolecular
462 Engineering at the Georgia Institute of Technology, for the calculation of aerosol pH and liquid water content.

463 **Competing interests.** The authors declare that they have no conflict of interests.

464 **Financial support.** This research was supported by National Natural Science Foundation of China (Grant Number:
465 41875155, 41605114, 41875174) and the Overseas Joint Training Program for Doctoral Students of Ocean
466 University of China. D.Z. was supported by JSPS KAKENHI 21H01158.

467 **References**

- 468 Arimoto, R., Zhang, X. Y., Huebert, B. J., Kang, C. H., Savoie, D. L., Prospero, J. M., Sage, S. K., Schloesslin, C.
469 A., Khaing, H. M., and Oh, S. N.: Chemical composition of atmospheric aerosols from Zhenbeitai, China,
470 and Gosan, South Korea, during ACE-Asia, *Journal of Geophysical Research: Atmospheres*, 109,
471 10.1029/2003JD004323, 2004.
- 472 Baldo, C., Ito, A., Krom, M. D., Li, W., Jones, T., Drake, N., Ignatyev, K., Davidson, N., and Shi, Z.: Iron from
473 coal combustion particles dissolves much faster than mineral dust under simulated atmospheric acidic
474 conditions, *Atmos. Chem. Phys.*, 22, 6045–6066, 10.5194/acp-22-6045-2022, 2022.
- 475 Chen, H. and Grassian, V. H.: Iron Dissolution of Dust Source Materials during Simulated Acidic Processing: The
476 Effect of Sulfuric, Acetic, and Oxalic Acids, *Environ. Sci. Technol.*, 47, 10312–10321, 10.1021/es401285s,
477 2013.
- 478 Chen, Y. and Siefert, R. L.: Seasonal and spatial distributions and dry deposition fluxes of atmospheric total and
479 labile iron over the tropical and subtropical North Atlantic Ocean, *Journal of Geophysical Research:*
480 *Atmospheres*, 109, <https://doi.org/10.1029/2003JD003958>, 2004.
- 481 Dou, J., Alpert, P. A., Corral Arroyo, P., Luo, B., Schneider, F., Xto, J., Huthwelker, T., Borca, C. N., Henzler, K.
482 D., Raabe, J., Watts, B., Herrmann, H., Peter, T., Ammann, M., and Krieger, U. K.: Photochemical degradation

483 of iron(III) citrate/citric acid aerosol quantified with the combination of three complementary experimental
484 techniques and a kinetic process model, *Atmos. Chem. Phys.*, 21, 315–338, 10.5194/acp-21-315-2021, 2021.

485 Fu, H., Cwiertny, D. M., Carmichael, G. R., Scherer, M. M., and Grassian, V. H.: Photoreductive dissolution of
486 Fe-containing mineral dust particles in acidic media, *Journal of Geophysical Research: Atmospheres*, 115,
487 <https://doi.org/10.1029/2009JD012702>, 2010.

488 Fu, H., Lin, J., Shang, G., Dong, W., Grassian, V. H., Carmichael, G. R., Li, Y., and Chen, J.: Solubility of Iron
489 from Combustion Source Particles in Acidic Media Linked to Iron Speciation, *Environ. Sci. Technol.*, 46,
490 11119–11127, 10.1021/es302558m, 2012.

491 Guo, H., Otjes, R., Schlag, P., Kiendler-Scharr, A., Nenes, A., and Weber, R. J.: Effectiveness of ammonia reduction
492 on control of fine particle nitrate, *Atmos. Chem. Phys.*, 18, 12241–12256, 10.5194/acp-18-12241-2018, 2018.

493 Guo, H., Xu, L., Bougiatioti, A., Cerully, K. M., Capps, S. L., Hite Jr, J. R., Carlton, A. G., Lee, S. H., Bergin, M.
494 H., Ng, N. L., Nenes, A., and Weber, R. J.: Fine-particle water and pH in the southeastern United States,
495 *Atmos. Chem. Phys.*, 15, 5211–5228, <https://doi.org/10.5194/acp-15-5211-2015>, 2015.

496 Hennigan, C. J., Izumi, J., Sullivan, A. P., Weber, R. J., and Nenes, A.: A critical evaluation of proxy methods used
497 to estimate the acidity of atmospheric particles, *Atmos. Chem. Phys.*, 15, 2775–2790, 10.5194/acp-15-2775-
498 2015, 2015.

499 Hettiarachchi, E. and Rubasinghege, G.: Mechanistic Study on Iron Solubility in Atmospheric Mineral Dust
500 Aerosol: Roles of Titanium, Dissolved Oxygen, and Solar Flux in Solutions Containing Different Acid Anions,
501 *ACS Earth and Space Chemistry*, 4, 101–111, 10.1021/acsearthspacechem.9b00280, 2020.

502 Hettiarachchi, E., Hurab, O., and Rubasinghege, G.: Atmospheric Processing and Iron Mobilization of Ilmenite:
503 Iron-Containing Ternary Oxide in Mineral Dust Aerosol, *The Journal of Physical Chemistry A*, 122, 1291–
504 1302, 10.1021/acs.jpca.7b11320, 2018.

505 Hettiarachchi, E., Reynolds, R. L., Goldstein, H. L., Moskowitz, B., and Rubasinghege, G.: Bioavailable iron
506 production in airborne mineral dust: Controls by chemical composition and solar flux, *Atmos. Environ.*, 205,
507 90–102, <https://doi.org/10.1016/j.atmosenv.2019.02.037>, 2019.

508 Hou, L., Dai, Q., Song, C., Liu, B., Guo, F., Dai, T., Li, L., Liu, B., Bi, X., Zhang, Y., and Feng, Y.: Revealing
509 Drivers of Haze Pollution by Explainable Machine Learning, *Environmental Science & Technology Letters*,
510 9, 112–119, 10.1021/acs.estlett.1c00865, 2022.

511 Huang, K., Zhuang, G., Li, J., Wang, Q., Sun, Y., Lin, Y., and Fu, J. S.: Mixing of Asian dust with pollution aerosol
512 and the transformation of aerosol components during the dust storm over China in spring 2007, *Journal of*
513 *Geophysical Research: Atmospheres*, 115, 10.1029/2009JD013145, 2010.

514 Li, J., Zhang, Y.-L., Cao, F., Zhang, W., Fan, M., Lee, X., and Michalski, G.: Stable Sulfur Isotopes Revealed a
515 Major Role of Transition-Metal Ion-Catalyzed SO₂ Oxidation in Haze Episodes, *Environ. Sci. Technol.*, 54,
516 2626–2634, <https://doi.org/10.1021/acs.est.9b07150>, 2020.

517 Li, K., Fang, X., Wang, T., Gong, K., Ali Tahir, M., Wang, W., Han, J., Cheng, H., Xu, G., and Zhang, L.:
518 Atmospheric organic complexation enhanced sulfate formation and iron dissolution on nano α -Fe₂O₃,
519 *Environmental Science: Nano*, 8, 698–710, 10.1039/D0EN01220C, 2021.

520 Li, R., Zhang, H., Wang, F., He, Y., Huang, C., Luo, L., Dong, S., Jia, X., and Tang, M.: Mass fractions, solubility,
521 speciation and isotopic compositions of iron in coal and municipal waste fly ash, *Science of The Total*
522 *Environment*, 838, 155974, <https://doi.org/10.1016/j.scitotenv.2022.155974>, 2022.

523 Li, W., Qi, Y., Qu, W., Qu, W., Shi, J., Zhang, D., Liu, Y., Zhang, Y., Zhang, W., Ren, D., Ma, Y., Wang, X., Yi, L.,
524 Sheng, L., and Zhou, Y.: PM_{2.5} source apportionment identified with total and soluble elements in positive
525 matrix factorization, *Sci. Total Environ.*, 858, 159948, <https://doi.org/10.1016/j.scitotenv.2022.159948>,

526 2023a.

527 Li, W., Qi, Y., Qu, W., Qu, W., Shi, J., Zhang, D., Liu, Y., Wu, F., Ma, Y., Zhang, Y., Ren, D., Du, X., Yang, S.,
528 Wang, X., Yi, L., Gao, X., Wang, W., Ma, Y., Sheng, L., and Zhou, Y.: Sulfate and nitrate elevation in reverse-
529 transport dust plumes over coastal areas of China, *Atmos. Environ.*, 295, 119518,
530 <https://doi.org/10.1016/j.atmosenv.2022.119518>, 2023b.

531 Li, W., Xu, L., Liu, X., Zhang, J., Lin, Y., Yao, X., Gao, H., Zhang, D., Chen, J., Wang, W., Harrison, R. M., Zhang,
532 X., Shao, L., Fu, P., Nenes, A., and Shi, Z.: Air pollution–aerosol interactions produce more bioavailable iron
533 for ocean ecosystems, *Sci. Adv.*, 3, e1601749, [10.1126/sciadv.1601749](https://doi.org/10.1126/sciadv.1601749), 2017.

534 Liu, L., Lin, Q., Liang, Z., Du, R., Zhang, G., Zhu, Y., Qi, B., Zhou, S., and Li, W.: Variations in concentration and
535 solubility of iron in atmospheric fine particles during the COVID-19 pandemic: An example from China,
536 *Gondwana Research*, 97, 138–144, <https://doi.org/10.1016/j.gr.2021.05.022>, 2021a.

537 Liu, M., Song, Y., Zhou, T., Xu, Z., Yan, C., Zheng, M., Wu, Z., Hu, M., Wu, Y., and Zhu, T.: Fine particle pH
538 during severe haze episodes in northern China, *Geophys. Res. Lett.*, 44, 5213–5221,
539 <https://doi.org/10.1002/2017GL073210>, 2017.

540 Liu, P., Ye, C., Xue, C., Zhang, C., Mu, Y., and Sun, X.: Formation mechanisms of atmospheric nitrate and sulfate
541 during the winter haze pollution periods in Beijing: gas-phase, heterogeneous and aqueous-phase chemistry,
542 *Atmos. Chem. Phys.*, 20, 4153–4165, [10.5194/acp-20-4153-2020](https://doi.org/10.5194/acp-20-4153-2020), 2020.

543 Liu, T., Chan, A. W. H., and Abbatt, J. P. D.: Multiphase Oxidation of Sulfur Dioxide in Aerosol Particles:
544 Implications for Sulfate Formation in Polluted Environments, *Environ. Sci. Technol.*, 55, 4227–4242,
545 [10.1021/acs.est.0c06496](https://doi.org/10.1021/acs.est.0c06496), 2021b.

546 Lueder, U., Jørgensen, B. B., Kappler, A., and Schmidt, C.: Photochemistry of iron in aquatic environments,
547 *Environmental Science: Processes & Impacts*, 22, 12–24, [10.1039/C9EM00415G](https://doi.org/10.1039/C9EM00415G), 2020.

548 Martin, J. H., Coale, K. H., Johnson, K. S., Fitzwater, S. E., Gordon, R. M., Tanner, S. J., Hunter, C. N., Elrod, V.
549 A., Nowicki, J. L., Coley, T. L., Barber, R. T., Lindley, S., Watson, A. J., Van Scoy, K., Law, C. S., Liddicoat,
550 M. I., Ling, R., Stanton, T., Stockel, J., Collins, C., Anderson, A., Bidigare, R., Ondrusek, M., Latasa, M.,
551 Millero, F. J., Lee, K., Yao, W., Zhang, J. Z., Friederich, G., Sakamoto, C., Chavez, F., Buck, K., Kolber, Z.,
552 Greene, R., Falkowski, P., Chisholm, S. W., Hoge, F., Swift, R., Yungel, J., Turner, S., Nightingale, P., Hatton,
553 A., Liss, P., and Tindale, N. W.: Testing the iron hypothesis in ecosystems of the equatorial Pacific Ocean,
554 *Nature*, 371, 123–129, [10.1038/371123a0](https://doi.org/10.1038/371123a0), 1994.

555 Oakes, M., Ingall, E. D., Lai, B., Shafer, M. M., Hays, M. D., Liu, Z. G., Russell, A. G., and Weber, R. J.: Iron
556 Solubility Related to Particle Sulfur Content in Source Emission and Ambient Fine Particles, *Environ. Sci.*
557 *Technol.*, 46, 6637–6644, [10.1021/es300701c](https://doi.org/10.1021/es300701c), 2012.

558 Pang, H., Zhang, Q., Wang, H., Cai, D., Ma, Y., Li, L., Li, K., Lu, X., Chen, H., Yang, X., and Chen, J.:
559 Photochemical Aging of Guaiacol by Fe(III)–Oxalate Complexes in Atmospheric Aqueous Phase, *Environ.*
560 *Sci. Technol.*, 53, 127–136, [10.1021/acs.est.8b04507](https://doi.org/10.1021/acs.est.8b04507), 2019.

561 Pye, H. O. T., Nenes, A., Alexander, B., Ault, A. P., Barth, M. C., Clegg, S. L., Collett Jr, J. L., Fahey, K. M.,
562 Hennigan, C. J., Herrmann, H., Kanakidou, M., Kelly, J. T., Ku, I. T., McNeill, V. F., Riemer, N., Schaefer,
563 T., Shi, G., Tilgner, A., Walker, J. T., Wang, T., Weber, R., Xing, J., Zaveri, R. A., and Zuend, A.: The acidity
564 of atmospheric particles and clouds, *Atmos. Chem. Phys.*, 20, 4809–4888, [10.5194/acp-20-4809-2020](https://doi.org/10.5194/acp-20-4809-2020), 2020.

565 Sakata, K., Kurisu, M., Takeichi, Y., Sakaguchi, A., Tanimoto, H., Tamenori, Y., Matsuki, A., and Takahashi, Y.:
566 Iron (Fe) speciation in size-fractionated aerosol particles in the Pacific Ocean: The role of organic
567 complexation of Fe with humic-like substances in controlling Fe solubility, *Atmos. Chem. Phys.*, 22, 9461–
568 9482, [10.5194/acp-22-9461-2022](https://doi.org/10.5194/acp-22-9461-2022), 2022.

569 Shi, J.-H., Zhang, J., Gao, H.-W., Tan, S.-C., Yao, X.-H., and Ren, J.-L.: Concentration, solubility and deposition
570 flux of atmospheric particulate nutrients over the Yellow Sea, *Deep Sea Research Part II: Topical Studies in*
571 *Oceanography*, 97, 43–50, <https://doi.org/10.1016/j.dsr2.2013.05.004>, 2013.

572 Shi, J., Guan, Y., Gao, H., Yao, X., Wang, R., and Zhang, D.: Aerosol Iron Solubility Specification in the Global
573 Marine Atmosphere with Machine Learning, *Environ. Sci. Technol.*, 56, 16453–16461,
574 10.1021/acs.est.2c05266, 2022.

575 Shi, J., Guan, Y., Ito, A., Gao, H., Yao, X., Baker, A. R., and Zhang, D.: High Production of Soluble Iron Promoted
576 by Aerosol Acidification in Fog, *Geophys. Res. Lett.*, 47, e2019GL086124,
577 <https://doi.org/10.1029/2019GL086124>, 2020.

578 Shi, Z., Krom, M. D., Jickells, T. D., Bonneville, S., Carslaw, K. S., Mihalopoulos, N., Baker, A. R., and Benning,
579 L. G.: Impacts on iron solubility in the mineral dust by processes in the source region and the atmosphere: A
580 review, *Aeolian Research*, 5, 21–42, <https://doi.org/10.1016/j.aeolia.2012.03.001>, 2012.

581 Shi, Z. B., Krom, M. D., Bonneville, S., and Benning, L. G.: Atmospheric Processing Outside Clouds Increases
582 Soluble Iron in Mineral Dust, *Environ. Sci. Technol.*, 49, 1472–1477, 10.1021/es504623x, 2015.

583 Solmon, F., Chuang, P. Y., Meskhidze, N., and Chen, Y.: Acidic processing of mineral dust iron by anthropogenic
584 compounds over the north Pacific Ocean, *Journal of Geophysical Research: Atmospheres*, 114,
585 <https://doi.org/10.1029/2008JD010417>, 2009.

586 Song, S., Gao, M., Xu, W., Shao, J., Shi, G., Wang, S., Wang, Y., Sun, Y., and McElroy, M. B.: Fine-particle pH
587 for Beijing winter haze as inferred from different thermodynamic equilibrium models, *Atmos. Chem. Phys.*,
588 18, 7423–7438, 10.5194/acp-18-7423-2018, 2018.

589 Sorooshian, A., Wang, Z., Coggon, M. M., Jonsson, H. H., and Ervens, B.: Observations of Sharp Oxalate
590 Reductions in Stratocumulus Clouds at Variable Altitudes: Organic Acid and Metal Measurements During the
591 2011 E-PEACE Campaign, *Environ. Sci. Technol.*, 47, 7747–7756, 10.1021/es4012383, 2013.

592 Sugie, K., Nishioka, J., Kuma, K., Volkov, Y. N., and Nakatsuka, T.: Availability of particulate Fe to phytoplankton
593 in the Sea of Okhotsk, *Mar. Chem.*, 152, 20–31, <https://doi.org/10.1016/j.marchem.2013.03.005>, 2013.

594 Sun, P., Nie, W., Chi, X., Xie, Y., Huang, X., Xu, Z., Qi, X., Xu, Z., Wang, L., Wang, T., Zhang, Q., and Ding, A.:
595 Two years of online measurement of fine particulate nitrate in the western Yangtze River Delta: influences of
596 thermodynamics and N₂O₅ hydrolysis, *Atmos. Chem. Phys.*, 18, 17177–17190, [https://doi.org/10.5194/acp-](https://doi.org/10.5194/acp-18-17177-2018)
597 18-17177-2018, 2018.

598 Tao, W., Su, H., Zheng, G., Wang, J., Wei, C., Liu, L., Ma, N., Li, M., Zhang, Q., Pöschl, U., and Cheng, Y.:
599 Aerosol pH and chemical regimes of sulfate formation in aerosol water during winter haze in the North China
600 Plain, *Atmos. Chem. Phys.*, 20, 11729–11746, 10.5194/acp-20-11729-2020, 2020.

601 Tobo, Y., Zhang, D., Matsuki, A., and Iwasaka, Y.: Asian dust particles converted into aqueous droplets under
602 remote marine atmospheric conditions, *Proc. Natl. Acad. Sci. U.S.A.*, 107, 17905, 2010.

603 Toner, B. M.: An improved model of the ocean iron cycle, *NATURE*, 620, 41–42, [https://doi.org/10.1038/d41586-](https://doi.org/10.1038/d41586-023-02406-x)
604 023-02406-x, 2023.

605 Turpin, B. J. and Lim, H.-J.: Species Contributions to PM_{2.5} Mass Concentrations: Revisiting Common
606 Assumptions for Estimating Organic Mass, *Aerosol Science and Technology*, 35, 602–610,
607 10.1080/02786820119445, 2001.

608 Wang, G., Tao, Y., Chen, J., Liu, C., Qin, X., Li, H., Yun, L., Zhang, M., Zheng, H., Gui, H., Liu, J., Huo, J., Fu,
609 Q., Deng, C., and Huang, K.: Quantitative Decomposition of Influencing Factors to Aerosol pH Variation
610 over the Coasts of the South China Sea, East China Sea, and Bohai Sea, *Environmental Science & Technology*
611 *Letters*, 9, 815–821, <https://doi.org/10.1021/acs.estlett.2c00527>, 2022.

612 Wang, G., Zhang, R., Gomez, M. E., Yang, L., Zamora, M. L., Hu, M., Lin, Y., Peng, J., Guo, S., Meng, J., Li, J.,
613 Cheng, C., Hu, T., Ren, Y., Wang, Y., Gao, J., Cao, J., An, Z., Zhou, W., Li, G., Wang, J., Tian, P., Marrero-
614 Ortiz, W., Secrest, J., Du, Z., Zheng, J., Shang, D., Zeng, L., Shao, M., Wang, W., Huang, Y., Wang, Y., Zhu,
615 Y., Li, Y., Hu, J., Pan, B., Cai, L., Cheng, Y., Ji, Y., Zhang, F., Rosenfeld, D., Liss, P. S., Duce, R. A., Kolb, C.
616 E., and Molina, M. J.: Persistent sulfate formation from London Fog to Chinese haze, *Proc. Natl. Acad. Sci.*
617 *U.S.A.*, 113, 13630, 2016.

618 Wang, H., Ding, J., Xu, J., Wen, J., Han, J., Wang, K., Shi, G., Feng, Y., Ivey, C. E., Wang, Y., Nenes, A., Zhao,
619 Q., and Russell, A. G.: Aerosols in an arid environment: The role of aerosol water content, particulate acidity,
620 precursors, and relative humidity on secondary inorganic aerosols, *Science of The Total Environment*, 646,
621 564–572, <https://doi.org/10.1016/j.scitotenv.2018.07.321>, 2019.

622 Wang, J., Zhao, B., Wang, S., Yang, F., Xing, J., Morawska, L., Ding, A., Kulmala, M., Kerminen, V.-M., Kujansuu,
623 J., Wang, Z., Ding, D., Zhang, X., Wang, H., Tian, M., Petäjä, T., Jiang, J., and Hao, J.: Particulate matter
624 pollution over China and the effects of control policies, *Science of The Total Environment*, 584–585, 426–
625 447, <https://doi.org/10.1016/j.scitotenv.2017.01.027>, 2017.

626 Wang, Q., Zhuang, G., Li, J., Huang, K., Zhang, R., Jiang, Y., Lin, Y., and Fu, J. S.: Mixing of dust with pollution
627 on the transport path of Asian dust - Revealed from the aerosol over Yulin, the north edge of Loess Plateau,
628 *Sci. Total Environ.*, 409, 573, 2011.

629 Wang, R., Balkanski, Y., Boucher, O., Bopp, L., Chappell, A., Ciais, P., Hauglustaine, D., Peñuelas, J., and Tao, S.:
630 Sources, transport and deposition of iron in the global atmosphere, *Atmos. Chem. Phys.*, 15, 6247–6270,
631 10.5194/acp-15-6247-2015, 2015.

632 Wang, X., Wei, W., Cheng, S., Zhang, H., and Yao, S.: Source estimation of SO_4^{2-} and NO_3^- based on monitoring-
633 modeling approach during winter and summer seasons in Beijing and Tangshan, China, *Atmos. Environ.*, 214,
634 116849, <https://doi.org/10.1016/j.atmosenv.2019.116849>, 2019.

635 Wang, Y., Hu, M., Hu, W., Zheng, J., Niu, H., Fang, X., Xu, N., Wu, Z., Guo, S., Wu, Y., Chen, W., Lu, S., Shao,
636 M., Xie, S., Luo, B., and Zhang, Y.: Secondary Formation of Aerosols Under Typical High-Humidity
637 Conditions in Wintertime Sichuan Basin, China: A Contrast to the North China Plain, *J. Phys. Chem. A*, 126,
638 e2021JD034560, <https://doi.org/10.1029/2021JD034560>, 2021.

639 Watson, A. J. and Lefèvre, N.: The sensitivity of atmospheric CO_2 concentrations to input of iron to the oceans,
640 *Tellus B: Chemical and Physical Meteorology*, 51, 453–460, 10.3402/tellusb.v51i2.16320, 1999.

641 Watson, A. J., Law, C. S., Van Scoy, K. A., Millero, F. J., Yao, W., Friederich, G. E., Liddicoat, M. I., Wanninkhof,
642 R. H., Barber, R. T., and Coale, K. H.: Minimal effect of iron fertilization on sea-surface carbon dioxide
643 concentrations, *Nature*, 371, 143–145, 10.1038/371143a0, 1994.

644 Weller, C., Tilgner, A., Bräuer, P., and Herrmann, H.: Modeling the Impact of Iron–Carboxylate Photochemistry
645 on Radical Budget and Carboxylate Degradation in Cloud Droplets and Particles, *Environ. Sci. Technol.*, 48,
646 5652–5659, 10.1021/es4056643, 2014.

647 Wong, J. P. S., Yang, Y., Fang, T., Mulholland, J. A., Russell, A. G., Ebel, S., Nenes, A., and Weber, R. J.: Fine
648 Particle Iron in Soils and Road Dust Is Modulated by Coal-Fired Power Plant Sulfur, *Environ. Sci. Technol.*,
649 54, 7088–7096, 10.1021/acs.est.0c00483, 2020.

650 Wu, C. and Yu, J. Z.: Evaluation of linear regression techniques for atmospheric applications: the importance of
651 appropriate weighting, *Atmos. Meas. Tech.*, 11, 1233–1250, 10.5194/amt-11-1233-2018, 2018.

652 Wu, Y., Ge, X., Wang, J., Shen, Y., Ye, Z., Ge, S., Wu, Y., Yu, H., and Chen, M.: Responses of secondary aerosols
653 to relative humidity and photochemical activities in an industrialized environment during late winter, *Atmos.*
654 *Environ.*, 193, 66–78, <https://doi.org/10.1016/j.atmosenv.2018.09.008>, 2018a.

655 Wu, Z., Wang, Y., Tan, T., Zhu, Y., Li, M., Shang, D., Wang, H., Lu, K., Guo, S., Zeng, L., and Zhang, Y.: Aerosol
656 Liquid Water Driven by Anthropogenic Inorganic Salts: Implying Its Key Role in Haze Formation over the
657 North China Plain, *Environmental Science & Technology Letters*, 5, 160–166, 10.1021/acs.estlett.8b00021,
658 2018b.

659 Xie, T., Lu, S., Zeng, J., Rao, L., Wang, X., Win, M. S., Zhang, D., Lu, H., Liu, X., and Wang, Q.: Soluble Fe
660 release from iron-bearing clay mineral particles in acid environment and their oxidative potential, *Science of*
661 *The Total Environment*, 726, 138650, <https://doi.org/10.1016/j.scitotenv.2020.138650>, 2020.

662 Xu, J., Chen, J., Zhao, N., Wang, G., Yu, G., Li, H., Huo, J., Lin, Y., Fu, Q., Guo, H., Deng, C., Lee, S. H., Chen,
663 J., and Huang, K.: Importance of gas-particle partitioning of ammonia in haze formation in the rural
664 agricultural environment, *Atmos. Chem. Phys.*, 20, 7259–7269, 10.5194/acp-20-7259-2020, 2020.

665 Yang, T., Chen, Y., Zhou, S., Li, H., Wang, F., and Zhu, Y.: Solubilities and deposition fluxes of atmospheric Fe
666 and Cu over the Northwest Pacific and its marginal seas, *Atmos. Environ.*, 239, 117763,
667 <https://doi.org/10.1016/j.atmosenv.2020.117763>, 2020.

668 Zhang, G., Lin, Q., Peng, L., Yang, Y., Jiang, F., Liu, F., Song, W., Chen, D., Cai, Z., Bi, X., Miller, M., Tang, M.,
669 Huang, W., Wang, X., Peng, P. a., and Sheng, G.: Oxalate Formation Enhanced by Fe-Containing Particles
670 and Environmental Implications, *Environ. Sci. Technol.*, 53, 1269–1277, 10.1021/acs.est.8b05280, 2019.

671 Zhang, H., Li, R., Dong, S., Wang, F., Zhu, Y., Meng, H., Huang, C., Ren, Y., Wang, X., Hu, X., Li, T., Peng, C.,
672 Zhang, G., Xue, L., Wang, X., and Tang, M.: Abundance and Fractional Solubility of Aerosol Iron During
673 Winter at a Coastal City in Northern China: Similarities and Contrasts Between Fine and Coarse Particles,
674 *Journal of Geophysical Research: Atmospheres*, 127, e2021JD036070,
675 <https://doi.org/10.1029/2021JD036070>, 2022.

676 Zhang, Z., Boxall, C., and Kelsall, G. H.: Photoelectrophoresis of colloidal iron oxides 1. Hematite (α -Fe₂O₃), in:
677 *Colloids in the Aquatic Environment*, edited by: Tadros, T. F., and Gregory, J., Elsevier, Oxford, 145–163,
678 <https://doi.org/10.1016/B978-1-85861-038-2.50014-0>, 1993.

679 Zhou, M., Zhang, Y., Han, Y., Wu, J., Du, X., Xu, H., Feng, Y., and Han, S.: Spatial and temporal characteristics
680 of PM_{2.5} acidity during autumn in marine and coastal area of Bohai Sea, China, based on two-site contrast,
681 *Atmos. Res.*, 202, 196–204, <https://doi.org/10.1016/j.atmosres.2017.11.014>, 2018.

682 Zhou, Y., Zhang, Y., Griffith, S. M., Wu, G., Li, L., Zhao, Y., Li, M., Zhou, Z., and Yu, J. Z.: Field Evidence of Fe-
683 Mediated Photochemical Degradation of Oxalate and Subsequent Sulfate Formation Observed by Single
684 Particle Mass Spectrometry, *Environ. Sci. Technol.*, 54, 6562–6574, 10.1021/acs.est.0c00443, 2020.

685 Zhu, X., Prospero, J. M., Savoie, D. L., Millero, F. J., Zika, R. G., and Saltzman, E. S.: Photoreduction of iron(III)
686 in marine mineral aerosol solutions, *Journal of Geophysical Research: Atmospheres*, 98, 9039–9046,
687 <https://doi.org/10.1029/93JD00202>, 1993.

688 Zhu, X. R., Prospero, J. M., and Millero, F. J.: Diel variability of soluble Fe(II) and soluble total Fe in North
689 African dust in the trade winds at Barbados, *Journal of Geophysical Research: Atmospheres*, 102, 21297–
690 21305, <https://doi.org/10.1029/97JD01313>, 1997.

691 Zhu, Y., Li, W., Lin, Q., Yuan, Q., Liu, L., Zhang, J., Zhang, Y., Shao, L., Niu, H., Yang, S., and Shi, Z.: Iron
692 solubility in fine particles associated with secondary acidic aerosols in east China, *Environmental Pollution*,
693 264, 114769, <https://doi.org/10.1016/j.envpol.2020.114769>, 2020.

694 Zhuang, G., Yi, Z., Duce, R. A., and Brown, P. R.: Link between iron and sulphur cycles suggested by detection
695 of Fe(n) in remote marine aerosols, *Nature*, 355, 537–539, 10.1038/355537a0, 1992.

696 Zuo, Y. and Hoigne, J.: Formation of hydrogen peroxide and depletion of oxalic acid in atmospheric water by
697 photolysis of iron(III)-oxalato complexes, *Environ. Sci. Technol.*, 26, 1014–1022, 10.1021/es00029a022,

698 1992.
699 Wang, H., Ding, J., Xu, J., Wen, J., Han, J., Wang, K., Shi, G., Feng, Y., Ivey, C. E., Wang, Y., Nenes, A., Zhao,
700 Q., and Russell, A. G.: Aerosols in an arid environment: The role of aerosol water content, particulate acidity,
701 precursors, and relative humidity on secondary inorganic aerosols, *Science of The Total Environment*, 646,
702 564-572, <https://doi.org/10.1016/j.scitotenv.2018.07.321>, 2019.
703 Zhang, G., Lin, Q., Peng, L., Yang, Y., Jiang, F., Liu, F., Song, W., Chen, D., Cai, Z., Bi, X., Miller, M., Tang, M.,
704 Huang, W., Wang, X., Peng, P. a., and Sheng, G.: Oxalate Formation Enhanced by Fe-Containing Particles
705 and Environmental Implications, *Environ. Sci. Technol.*, 53, 1269-1277, 10.1021/acs.est.8b05280, 2019.
706 Sun, P., Nie, W., Chi, X., Xie, Y., Huang, X., Xu, Z., Qi, X., Xu, Z., Wang, L., Wang, T., Zhang, Q., and Ding, A.:
707 Two years of online measurement of fine particulate nitrate in the western Yangtze River Delta: influences of
708 thermodynamics and N₂O₅ hydrolysis, *Atmos. Chem. Phys.*, 18, 17177-17190, 10.5194/acp-18-17177-2018,
709 2018.
710